

Uncertainty analysis and robust trajectory linearization control of a flexible air-breathing hypersonic vehicle

Zhiqiang Pu, Xiangmin Tan*, Guoliang Fan, Jianqiang Yi

Institute of Automation, Chinese Academy of Sciences, No. 95 Zhongguancun East Road, Haidian District, Beijing 100190, China

ARTICLE INFO

Article history:

Received 23 May 2013

Received in revised form

20 November 2013

Accepted 27 January 2014

Available online 3 February 2014

Keywords:

Uncertainty

Flexible

Hypersonic vehicle

Trajectory linearization control

Extended state observer

ABSTRACT

Flexible air-breathing hypersonic vehicles feature significant uncertainties which pose huge challenges to robust controller designs. In this paper, four major categories of uncertainties are analyzed, that is, uncertainties associated with flexible effects, aerodynamic parameter variations, external environmental disturbances, and control-oriented modeling errors. A uniform nonlinear uncertainty model is explored for the first three uncertainties which lumps all uncertainties together and consequently is beneficial for controller synthesis. The fourth uncertainty is additionally considered in stability analysis. Based on these analyses, the starting point of the control design is to decompose the vehicle dynamics into five functional subsystems. Then a robust trajectory linearization control (TLC) scheme consisting of five robust subsystem controllers is proposed. In each subsystem controller, TLC is combined with the extended state observer (ESO) technique for uncertainty compensation. The stability of the overall closed-loop system with the four aforementioned uncertainties and additional singular perturbations is analyzed. Particularly, the stability of nonlinear ESO is also discussed from a Liénard system perspective. At last, simulations demonstrate the great control performance and the uncertainty rejection ability of the robust scheme.

© 2014 Published by Elsevier Ltd. on behalf of IAA.

1. Introduction

Air-breathing hypersonic vehicles are viewed as a reliable and cost-effective solution to access the space routine. Since the 1960s, considerable effort has been made to develop practical and affordable vehicles. Recent achievements include the successful flight tests of NASA X-43A [1] and U.S. Air Force X-51A [2]. However, the design of robust guidance and control systems is still a challenging task due to complex coupling effects and significant uncertainties [3–8]. Hypersonic flight usually covers a large flight envelope during which the environmental and aerodynamic characteristics undergo huge

variations. The slender geometries and light structures required for these aircraft cause significant uncertain flexible effects. Strong interactions also exist among propulsion, structure, aerodynamics, and control. In addition, the lack of experimental data makes the vehicle model far less accurate [9–16].

In the recent literature, there are two dominant flexible air-breathing hypersonic vehicle (FAHV) models: one is the first-principle model developed by Bolender and Doman [3,4], the other is the computational fluid dynamics (CFD) based model of Mirmirani et al. [5]. Based on these models, diverse control systems are designed with varying levels of model fidelity. For the first model, linear approaches were applied for control design in [8–10] based on model linearization around trim conditions. In these cases, strategies in the frequency domain could be easily applied to evaluate the linear approaches. However, gain scheduling was needed

* Corresponding author. Tel.: +86 010 82544639.

E-mail addresses: zhiqiang.pu@ia.ac.cn (Z. Pu),

xiangmin.tan@ia.ac.cn (X. Tan), guoliang.fan@ia.ac.cn (G. Fan),

jianqiang.yi@ia.ac.cn (J. Yi).

among the trim conditions for a large flight envelope, thus proof of the stability of the whole scheduled system became a challenging task. As for the nonlinear methods, feedback linearization [11], robust adaptive inversion-based design [12], and quasi-continuous high-order sliding mode approach [13] were proposed with less complex uncertainties than those considered in this paper. For the second model which is not discussed in this paper, Kuipers et al. [17] developed an adaptive linear quadratic controller, while Levin et al. [18] presented a control scheme that could suppress unknown or changing flexible modes online. Despite these research results, the design of robust control systems is still an open problem because of the peculiarity of the vehicle dynamics [12].

In the context of the aforementioned literature, the current research focus of FAHV is to design a controller that can achieve robust output tracking under diverse uncertainties. This problem is considered in many papers [9–16] with different kinds and varying levels of uncertainties. In [9–12], however, the uncertainties were only applied to test the system robustness. That means no particular technique was adopted to deal with uncertainties, and the uncertainty should be constrained within the stability domain of the closed-loop system. For a model based control method, in order to design a controller that owns the best uncertainty rejection ability, a valid uncertainty model is assumed to be available. Development of such a model, however, has received far less attention in the literature. Rehman et al. [14] developed an uncertainty model that considered 24 uncertain inertial and aerodynamic parameters. This model was chiefly based on mathematical computation to make feedback linearization applicable, but physical genesis of the uncertainties was not discussed. Buschek et al. [15] and Chavez et al. [16] presented another two uncertainty models which were only applicable to linear control law synthesis. In this paper, based on different physical and/or mathematical geneses, uncertainties are characterized by four types: flexibility effects, aerodynamic parameter uncertainties, external environmental disturbances, and control-oriented modeling errors. The first three uncertainties physically exist in vehicle dynamics, thus open-loop behaviors of FAHV with these uncertainties are analyzed, offering insights on the vehicle features and guidelines for control design. Based on the analysis, we develop a uniform nonlinear uncertainty model that is more realistic for FAHV. This model lumps all these three uncertainties together and is therefore beneficial for compensation design. This model also features two “disturbance-matching matrices” which clearly describe the physics of typical aerodynamic parameter uncertainties such as propulsive perturbations and variations in control effectiveness. The fourth uncertainty results from mathematical derivation of the control law design and is not included in the uncertainty model. However, it is considered in closed-loop stability analysis.

Based on the uncertainty analysis and modeling, we propose a robust control scheme that combines trajectory linearization control (TLC) [19–25] and extended state observer (ESO) [26–28]. As a novel nonlinear control approach, TLC can inherently guarantee the exponential stability of the closed-loop system along nominal trajectories using linear time-varying (LTV) system PD-spectral theory [29]. Moreover,

TLC provides a unique time-varying bandwidth (TVB) technique to feasibly improve control performance and system robustness. Because of its simplicity and inherent robustness, TLC has been applied to hypersonic vehicles [19–21], unmanned aircraft [24], and mobile robots [25]. In this paper, TLC is integrated with ESO for uncertainty estimation, forming a robust TLC scheme. By adopting simple nonlinear structures, ESO shows high estimation efficiency while maintaining good flexibility as the control scheme can be easily redesigned to determine whether ESO is used in one specific control channel or in all channels. In addition, its great simplicity can significantly shorten the computing time and meet the fast computation requirement in practical hypersonic missions, which is a great advantage over other time-consuming estimation techniques such as fuzzy logic and neural network.

To sum up, the objective of this paper is to design a robust TLC scheme for FAHV in the presence of multiple uncertainties. The paper is organized as follows. The FAHV motion equations, together with force/moment expressions, are given in Section 2. Uncertainty analysis and modeling are discussed in Section 3. Section 4 addresses the control scheme design. The vehicle dynamics are decomposed into five functional subsystems. In each subsystem, a basic TLC configuration, together with an adaptive TVB algorithm, is integrated with ESO for uncertainty estimation. Section 5 presents stability analysis of the perturbed closed-loop system, where the aforementioned uncertainties and additional singular perturbations are considered. The stability of nonlinear ESO is also analyzed in this section from a Liénard system perspective. Section 6 contains multiple simulations to show the effectiveness of the robust scheme. Finally conclusions are drawn in Section 7.

2. Vehicle model

The vehicle studied in this paper is the model developed by Bolender and Doman [3,4] for the longitudinal dynamics of a FAHV. Its sketch is illustrated in Fig. 1. Flexibility effects are included by modeling the fuselage as two cantilever beams clamped at the center of gravity, rather than a single free-free beam as done in [7–9]. This vibrational model captures the inertial coupling between the rigid-body states and the flexible states, resulting in a system that is more complex to control [4]. Assuming a flat Earth and normalizing the vehicle to unit depth, the equations of motion are written in the stability axes as [11]

$$\dot{V} = (T \cos \alpha - D)/m - g \sin \gamma \quad (1)$$

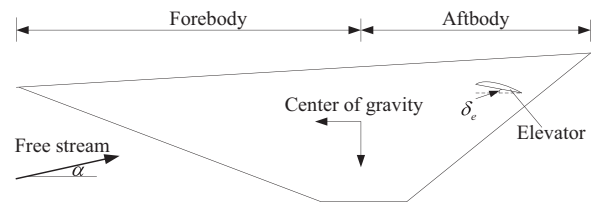


Fig. 1. Geometry of the hypersonic vehicle model.

$$\dot{\gamma} = (L + T \sin \alpha)/(mV) - g \cos \gamma / V \quad (2)$$

$$\dot{h} = V \sin \gamma \quad (3)$$

$$\dot{\alpha} = Q - \dot{\gamma} \quad (4)$$

$$I_{yy} \dot{Q} = M + \tilde{\psi}_f \ddot{\eta}_f + \tilde{\psi}_a \ddot{\eta}_a \quad (5)$$

$$k_f \ddot{\eta}_f = -2\xi_f \omega_f \dot{\eta}_f - \omega_f^2 \eta_f + N_f - \tilde{\psi}_f M / I_{yy} - \tilde{\psi}_f \tilde{\psi}_a \ddot{\eta}_a / I_{yy} \quad (6)$$

$$k_a \ddot{\eta}_a = -2\xi_a \omega_a \dot{\eta}_a - \omega_a^2 \eta_a + N_a - \tilde{\psi}_a M / I_{yy} - \tilde{\psi}_a \tilde{\psi}_f \ddot{\eta}_f / I_{yy} \quad (7)$$

This model is composed of five rigid-body states $x = [V, \gamma, h, \alpha, Q]^T$, where V , γ , h , α , and Q are the velocity, flight-path angle, altitude, angle of attack, and pitch rate, respectively. It also includes four flexible states $\eta = [\eta_f, \dot{\eta}_f, \eta_a, \dot{\eta}_a]^T$ which correspond to the first generalized elastic deformations and their derivatives of the forebody (denoted with subscript f) and aftbody (denoted with subscript a). The outputs to be controlled are selected as $y = [V, h]^T$. The elevator deflection δ_e and the fuel equivalence ratio ϕ constitute the control inputs $u = [\delta_e, \phi]^T$, which indirectly affect the vehicle states through the lift L , drag D , thrust T , pitching moment M , and the generalized forces N_f and N_a . Readers may refer to [11] for a full description of the model variables.

The aforementioned forces and moment are complex nonlinear functions of the vehicle states and control inputs, which makes the FAHV control design a challenging task. Based on the vehicle database, Parker et al. [11] developed a curve-fitted model (CFM) to approximate the forces and moment, which is described as

$$\begin{cases} L \approx \bar{q} SC_L(\alpha, \delta_e), & D \approx \bar{q} SC_D(\alpha, \delta_e) \\ T \approx C_T^3 \alpha^3 + C_T^2 \alpha^2 + C_T^1 \alpha + C_T^0 \\ M \approx z_T T + \bar{q} S [C_{M,\alpha}(\alpha) + C_{M,\delta_e}(\delta_e)] \\ N_f \approx N_f^2 \alpha^2 + N_f^1 \alpha + N_f^0 \\ N_a \approx N_a^2 \alpha^2 + N_a^1 \alpha + N_a^0 \delta_e + N_a^0 \end{cases} \quad (8)$$

The coefficients are expressed as

$$\begin{cases} C_L = C_L^\alpha \alpha + C_L^{\delta_e} \delta_e + C_L^0 \\ C_D = C_D^\alpha \alpha^2 + C_D^\alpha \alpha + C_D^{\delta_e} \delta_e^2 + C_D^{\delta_e} \delta_e + C_D^0 \\ C_{M,\alpha} = C_{M,\alpha}^2 \alpha^2 + C_{M,\alpha}^1 \alpha + C_{M,\alpha}^0, & C_{M,\delta_e} = C_{M,\delta_e} \delta_e \\ C_T^3 = \beta_1(h, \bar{q}) \phi + \beta_2(h, \bar{q}), & C_T^2 = \beta_3(h, \bar{q}) \phi + \beta_4(h, \bar{q}) \\ C_T^1 = \beta_5(h, \bar{q}) \phi + \beta_6(h, \bar{q}), & C_T^0 = \beta_7(h, \bar{q}) \phi + \beta_8(h, \bar{q}) \end{cases} \quad (9)$$

The numerical values of these coefficients can be found in [11]. The dynamic pressure is calculated as $\bar{q} = 0.5 \rho V^2$, where the air density ρ is modeled as $\rho = \rho_0 \exp(-h/h_0)$. Actuators are modeled as first-order low-pass filters with certain gains. Limits on the actuator outputs are set as

$$-15^\circ \leq \delta_e \leq 15^\circ, \quad 0.1 \leq \phi \leq 1.2 \quad (10)$$

3. Uncertainty analysis and modeling

3.1. Flexibility uncertainty

The slender geometries and light structures of FAHV cause significant flexibility effects that severely affect the

Table 1

Mass densities under varying fuel levels.

Fuel level	Case 1	Case 2	Case 3	Case 4
Mass (slugs/ft)	300	250	200	150

aerodynamics of the aircraft. However, due to lack of experimental data support, any assumed flexible mode η_i considered in the current model is imperfectly modeled, resulting in uncertainties of structural mode shape, vibration modal frequency ω_i , and damping ratio ξ_i . Here, for all modes the damping ratio is constant $\xi_i = 0.02$ as done in [8–10], which indicates a severe mode vibration condition. However, the other two factors may undergo huge variations. Particularly, the fuel is consumed during hypersonic flight, which generates significant uncertainties of the structural dynamics [7]. In the following analysis, we will find out how the mode shape and the frequency change with four different fuel levels. The corresponding vehicle mass densities are listed in Table 1.

In the nominal case (Case 1), mode shapes for the first three flexible modes are shown in Fig. 2a. It is seen that, as the fuselage is modeled as two cantilever beams clamped at the center of gravity (55 ft away from the nose), the displacement and rotation at the center of gravity are zero. This is different from the free-free model in [7–9]. Fig. 2b shows the second mode shape with mass density ranging from 300 slugs/ft to 150 slugs/ft. As a general rule, the displacement increases as the mass density decreases, resulting in changes of the vehicle dynamics. Besides the second mode shape, all other mode shapes lead to the same rule. This means that more fuel consumption or lighter vehicle structures cause larger flexibility effects.

As for the mode frequency, consider the frequency equation [3,4]:

$$\beta^4 = \omega^2 \hat{m} / (EI) \quad (11)$$

where ω is the mode frequency, \hat{m} is the mass density, and EI is regarded as a constant. β is also a constant, corresponding to the solution of the equation

$$\cos(\beta l) \cosh(\beta l) = -1 \quad (12)$$

where l is the beam length. In view of (11) and (12), we have

$$\omega^2 \propto 1 / \hat{m} \quad (13)$$

Thus, increased mass density leads to decreased flexible mode frequencies. If the decreasing flexible frequencies approach the natural frequency of the rigid body, significant coupling occurs and the vehicle dynamics become more complex.

The above analysis indicates that variations in the mass density may result in large uncertainties of mode shape and natural frequency. This flexibility uncertainty is labeled as Uncertainty 1 hereafter.

3.2. Environmental uncertainty

FAHV exhibits complex time-varying coupling effects not only between the rigid and flexible states, but also

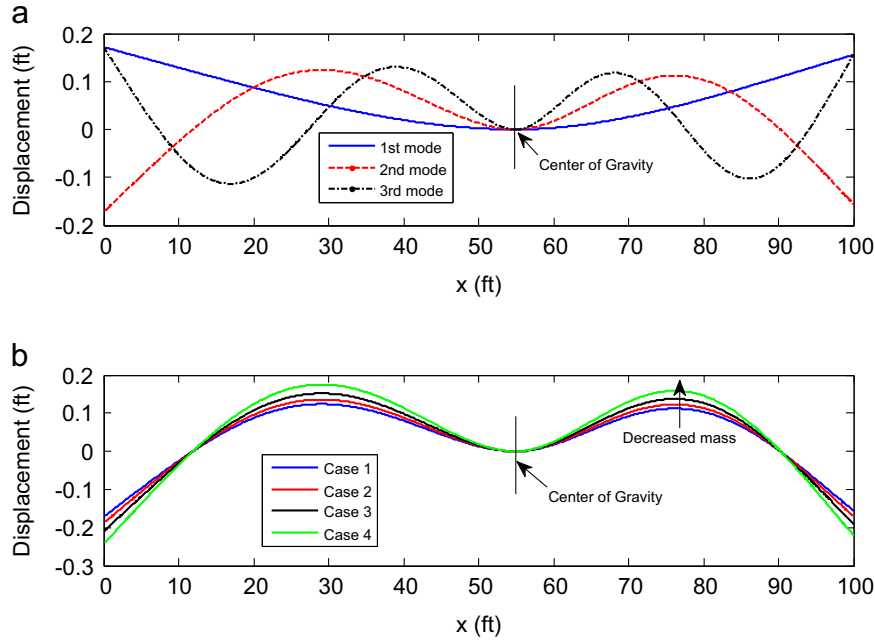


Fig. 2. Mode shapes: (a) the first three mode shapes in nominal case and (b) the second mode shape with varying mass densities.

Table 2

Open-loop eigenvalues of the linearized system.

Eigen value	Damping ratio	Natural freq. (rad/s)	Mode
$-0.354 \pm 17.7j$	0.02	17.7	Forebody flexibility
$-0.433 \pm 21.6j$	0.02	21.6	Aftbody flexibility
-1.78	1	1.78	Short period
1.71	-1	1.71	Short period
3.37×10^{-6}	-1	3.37×10^{-6}	Altitude
$-0.00809 \pm 0.0398j$	0.0203	0.0398	Phugoid

between the aerodynamics and the environment. As a key uncertainty factor, the variation of dynamic pressure \bar{q} influences all the forces and moment. For this reason, an open-loop analysis is conducted with \bar{q} ranging from 2000 psf to 500 psf. We trim the vehicle at each \bar{q} level, and then use the MATLAB function *linmod* (based on first-order Taylor expansion theory) to linearize the original model (1)–(7) around the trim conditions as

$$[\dot{x}, \dot{\eta}]^T = A[x, \eta]^T + Bu \quad (14)$$

Here, the values of the Jacobian matrices $A \in \mathbb{R}^{9 \times 9}$ and $B \in \mathbb{R}^{9 \times 2}$ are omitted for simplicity. For demonstration, the poles of the linearized open-loop model for dynamic pressure of 2000 psf are listed in Table 2. Fig. 3 shows how the poles and zeros migrate as \bar{q} changes. As expected, three poles corresponding to the phugoid and altitude modes are near the origin. The two complex conjugate pairs correspond to the flexible dynamics. It is seen that the varying \bar{q} almost has no impact on the flexible modes, which is primarily because the generalized forces N_f and N_a are modeled as independent of \bar{q} . The pair of poles that appear to be symmetric about the imaginary

axis correspond to the rotational dynamics (the angle of attack and pitch rate). The unstable pole complicates the control design. As the dynamic pressure decreases, both the positive and negative rotational poles migrate to the origin. This is reasonable because with a smaller \bar{q} all forces and moments decrease. On one hand, it makes the unstable dynamics much milder; on the other hand, it yields a larger oscillation in the stable dynamics. Finally, the positive zero indicates a nonminimum phase behavior, which stems from the coupling of the elevator to the lift and drag forces. This phenomenon was also reported in [11,12], where an additional canard was therefore added to deal with it.

Besides the dynamic pressure uncertainty, additional environmental uncertainties may result from wind gusts and other unpredictable factors. All these environmental uncertainties are labeled as Uncertainty 2 later.

3.3. Aerodynamic parameter uncertainty

FAHV typically utilizes a scramjet propulsion system which is highly integrated into the airframe. This results in an increased sensitivity to variations in the angle of attack. The most significant impact of this propulsive disturbance is on the pitching moment leading to large elevator deflection to stabilize the vehicle [15]. Thus, a typical aerodynamic uncertainty source is the parametric uncertainty of the coefficient $C_{m,\alpha}$. Fig. 4 shows the migrations of the poles and zeros with varying uncertainty levels of $C_{m,\alpha}$ ranging from +50 to -50% for a trim condition at Mach 8 and 85,000 ft. It is seen that the rotational dynamics are significantly affected. For a decreasing $C_{m,\alpha}$, both the poles and zeros of the rotational dynamics migrate to the origin. For example, with +50% uncertainty the unstable pole is located at 1.81 rad/s, while with -50% uncertainty it

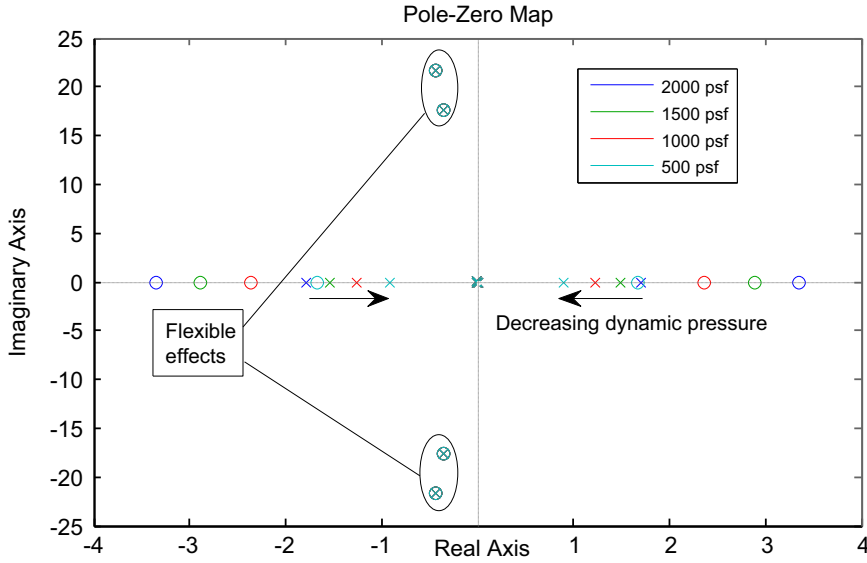


Fig. 3. Pole-zero map with varying dynamic pressures.

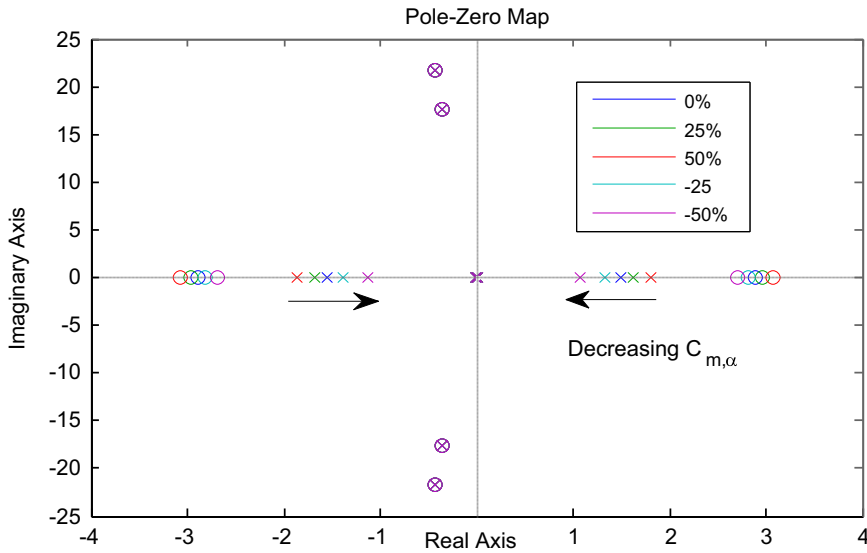


Fig. 4. Pole-zero map with varying uncertainty levels of $C_{m,\alpha}$.

migrates to 1.07 rad/s. This exhibits the same feature as that in the dynamic pressure variation analysis because both cases decrease the pitching moment as described in the term $\bar{q}S\bar{c}C_{m,\alpha}$. This indicates that the parameter uncertainty can seriously change the vehicle features and therefore make the control design much more challenging.

Parameter uncertainty is one of the most common issues in practical flight. To avoid clouding the main idea of this paper, we only take the propulsive disturbance just noted for demonstration to show the necessity of developing an uncertainty model to analyze its underlying physical influences to vehicle behaviors. Other typical uncertainties include variations in control effectiveness related to the two control variables: the elevator deflection

and the fuel equivalence ratio. All these uncertainties are labeled as Uncertainty 3 later.

3.4. Control-oriented modeling error

The aforementioned three uncertainties stem from the practical physical system of the vehicle. From a control-oriented perspective, one more uncertainty needs to be considered, that is, the control-oriented modeling error. This uncertainty results from the approximation and/or simplification during the controller design, and therefore is dependent on each specific control method. In TLC, the linearization errors during the stabilizing control law design need to be included. In addition, any approximation

for yielding an affine model to make TLC applicable is also viewed as an uncertainty source. These uncertainties are labeled as Uncertainty 4 and need to be considered for stability analysis.

3.5. Uncertainty modeling

Consider the rigid-body dynamics (1)–(5). All the flexibility uncertainties, as well as environment disturbances and aerodynamic parameter uncertainties, can be represented by the following uniform additive uncertainty model:

$$\dot{x} = f(x, u) + \underbrace{f_{\Delta 1}(x, u, t) + f_{\Delta 2}(x, u, t) + f_{\Delta 3}(x, u, t)}_{\Delta f} \quad (15)$$

where $\dot{x} = f(x, u)$ and $x, f(\cdot) \in \mathbb{R}^5$ denote the nominal dynamics, while $f_{\Delta 1}(x, u, t), f_{\Delta 2}(x, u, t), f_{\Delta 3}(x, u, t) \in \mathbb{R}^5$ denote Uncertainties 1, 2, and 3, respectively. Here we lump these uncertainties together in Δf , which is convenient to design an observer for uncertainty compensation. Uncertainty 4 is not included in Δf because, as already stated, it is artificially introduced during mathematical derivation of the controller design and therefore is determined by each specific control method. In this paper, this control-oriented modeling error should be overcome by the inherent controller robustness. However, it is considered in the closed-loop stability analysis addressed later.

For Uncertainty 1, $\pm 25\%$ uncertainties in mode shapes and modal frequencies are introduced, yielding $f_{\Delta 1}(x, u, t)$ implicitly. As for Uncertainty 2, environmental uncertainties considered in this paper include air density uncertainty, air temperature uncertainty, and unpredictable wind disturbances. Uncertainties of air density and temperature lead to an uncertainty of dynamic pressure, and then affect the vehicle behaviors as shown in Fig. 3. In addition, the uncertain air temperature also leads to an uncertain airspeed, and then the Mach number is uncertain, which brings uncertainties to all forces and moments. In this paper, $\pm 40\%$ uncertainties in air density and temperature are introduced, yielding $f_{\Delta 2}^1(x, u, t)$ and $f_{\Delta 2}^2(x, u, t)$ (the first two components of Uncertainty 2) implicitly. Wind disturbances may affect the body-axis velocities, and then affect other states. Two uncertainty cases are considered to describe diverse unpredictable wind disturbances. In the first case, a time-varying vector is directly added to the vehicle motion equations to describe the influences of wind gusts to each channel. For demonstration, this uncertainty (denoted as $f_{\Delta 2}^3(x, u, t)$) is chosen as sine wave signals [10]

$$f_{\Delta 2}^3(x, u, t) = [2 \sin t, 5 \cos t, 0.3 \sin t, 0.3 \sin t, 0.05 \sin t]^T \quad (16)$$

One advantage of modeling the wind gusts as (16) lies in the fact that if the uncertainty observing technique is applied (as done in this paper), it is quite convenient to validate the effectiveness of the observer in each channel using these explicit expressions. The other case of wind disturbances is modeled as a large instant disturbance to the pitching moment. This model captures features of unpredictable strong airflows that may only last several

seconds or even shorter. Under such strong airflows, the forebody and aftbody of the vehicle have quite different aerodynamic behaviors, yielding a large disturbance to the pitching moment. In such cases, the phugoid modes may not have huge variations, while the short period modes may be immediately disturbed. Here, assume that the pitching moment disturbance only lasts a short time interval $[t_1, t_r]$. It is modeled as the sum of a pulse signal with large amplitude M_w and a relatively small sine wave signal $A_w \sin(w_w t)$ with high frequency (10–20 Hz). Then the fourth environmental uncertainty (denoted as $f_{\Delta 2}^4(x, u, t)$) can be modeled as

$$f_{\Delta 2}^4(x, u, t) = [0, 0, 0, \Delta f_q]^T, \quad \text{where} \quad \Delta f_q = \begin{cases} (M_w + A_w \sin(w_w t))/I_{yy}, & t_1 \leq t \leq t_r \\ 0, & \text{other time} \end{cases} \quad (17)$$

To sum up, the total environmental uncertainty $f_{\Delta 2}(x, u, t)$ is modeled as

$$f_{\Delta 2}(x, u, t) = \sum_{j=1}^4 f_{\Delta 2}^j(x, u, t) \quad (18)$$

Modeling of Uncertainty 3 remains an important task because aerodynamic parameter uncertainty commonly exists in hypersonic flight. In view of (8) and (9), three variables that majorly determine the forces and pitching moment are the flight state α and the control inputs δ_e, ϕ . Each variation of these variables may separately generate several parameter uncertainty sources. For this complicated type of uncertainty, we intend to present a model that (a) has a unified form to cover all of these uncertainty sources; (b) can clearly describe the physical connections between the uncertainty sources and relevant disturbed vehicle dynamics, thus offering a better understanding of the vehicle behaviors; and (c) is beneficial for the validation of uncertainty rejection control laws. Following this idea, we present a novel uniform model for Uncertainty 3 as

$$f_{\Delta 3}(x, u, t) = \sum_{k=1}^{n_3} f_{\Delta 3}^k(x, u, t) \quad (19)$$

The total value $f_{\Delta 3}(x, u, t)$ of Uncertainty 3 is the sum of multiple uncertainty sources (denoting the total number of aerodynamic parameter uncertainty sources as n_3). For each uncertainty case $f_{\Delta 3}^k(x, u, t) \in \mathbb{R}^5$, it is modeled as

$$\begin{cases} e_{\Delta k} = A_{\Delta k}^T F_1(\Delta_{lk}) B_{\Delta k} \\ f_{\Delta 3}^k(x, u, t) = F_2(e_{\Delta k}) A_{\Delta k} \end{cases} \quad (20)$$

here, Δ_{lk} denotes the uncertainty level. $F_1 \in \mathbb{R}^{4 \times 3}$ and $F_2 \in \mathbb{R}^{5 \times 4}$ are two disturbance-matching matrices. F_1 describes how the three primary parameter uncertainty sources affect the four forces/moment $\{L, D, T, M\}$, while F_2 tells how the four forces/moment affect the five rigid-body dynamics. The vectors $A_{\Delta k} \in \mathbb{R}^4$ and $B_{\Delta k} \in \mathbb{R}^3$ are chosen to “pick out” the matched uncertainty source and the disturbed dynamics. Both F_1 and F_2 have fixed forms which are separately derived from the force/moment expressions (8) and (9) and the equations of motion (1) and (5). Removing the function arguments Δ_{lk} and $e_{\Delta k}$ for brevity,

we denote F_1 and F_2 as

$$F_1 = \begin{bmatrix} L_\alpha & L_{\delta_e} & 0 \\ D_\alpha & D_{\delta_e} & 0 \\ T_\alpha & 0 & T_\phi \\ M_\alpha & M_{\delta_e} & M_\phi \end{bmatrix}, \quad F_2 = \begin{bmatrix} 0 & V_D & V_T & 0 \\ \gamma_L & 0 & \gamma_T & 0 \\ 0 & 0 & 0 & 0 \\ \alpha_L & 0 & \alpha_T & 0 \\ 0 & 0 & 0 & Q_M \end{bmatrix} \quad (21)$$

The elements of F_1 are given as follows:

$$\begin{cases} L_\alpha(\Delta_{lk}) = \bar{q} S C_L^\alpha \alpha \Delta_{lk} \\ D_\alpha(\Delta_{lk}) = \bar{q} S (C_D^{\alpha^2} \alpha^2 + C_D^\alpha \alpha) \Delta_{lk} \\ T_\alpha(\Delta_{lk}) = (C_T^{\alpha^3} \alpha^3 + C_T^{\alpha^2} \alpha^2 + C_T^\alpha \alpha) \Delta_{lk} \\ M_\alpha(\Delta_{lk}) = [\bar{q} S C_{M,\alpha}^{\alpha^2} \alpha^2 + C_{M,\alpha}^\alpha \alpha + C_T^{\alpha^3} \alpha^3 + C_T^{\alpha^2} \alpha^2 + C_T^\alpha \alpha] \Delta_{lk} \\ L_{\delta_e}(\Delta_{lk}) = \bar{q} S C_L^{\delta_e} \delta_e \Delta_{lk} \\ D_{\delta_e}(\Delta_{lk}) = \bar{q} S (C_D^{\delta_e^2} \delta_e^2 + C_D^{\delta_e} \delta_e) \Delta_{lk} \\ M_{\delta_e}(\Delta_{lk}) = \bar{q} S C_{M,\delta_e} \delta_e \Delta_{lk} \\ T_\phi(\Delta_{lk}) = (\beta_1 \alpha^3 + \beta_3 \alpha^2 + \beta_5 \alpha + \beta_7) \phi \Delta_{lk} \\ M_\phi(\Delta_{lk}) = (\beta_1 \alpha^3 + \beta_3 \alpha^2 + \beta_5 \alpha + \beta_7) z_T \phi \Delta_{lk} \end{cases} \quad (22)$$

The elements of F_2 are given as follows:

$$\begin{cases} \gamma_L(e_{\Delta k}) = e_{\Delta k} / m V \\ \alpha_L(e_{\Delta k}) = -e_{\Delta k} / m V \\ V_D(e_{\Delta k}) = -e_{\Delta k} / m \\ V_T(e_{\Delta k}) = e_{\Delta k} \cos \alpha / m \\ \gamma_T(e_{\Delta k}) = e_{\Delta k} \sin \alpha / m V \\ \alpha_T(e_{\Delta k}) = -e_{\Delta k} \sin \alpha / m V \\ Q_M(e_{\Delta k}) = e_{\Delta k} / I_{yy} \end{cases} \quad (23)$$

It is seen that through the models (19)–(23), the physical connections of the uncertainty sources and the relevant disturbed dynamics can be clearly depicted. In addition, by setting different $A_{\Delta k}$ and $B_{\Delta k}$, either single or multiple uncertainties can be simply included. In this paper, three typical parameter uncertainties are considered: propulsive

uncertainty and control effectiveness variations related to elevator deflection and fuel equivalence ratio, which are separately denoted as $f_{\Delta 3}^1$, $f_{\Delta 3}^2$, and $f_{\Delta 3}^3$. As mentioned in the uncertainty analysis, the scramjet propulsion system of FAHV is highly integrated into the airframe. The variation of α has a great impact on the pitching moment, which is represented by M_α in F_1 . Furthermore, the disturbed pitching moment chiefly influences the pitch rate dynamics, which can be represented by Q_M in F_2 . Therefore, to model this propulsive uncertainty $f_{\Delta 3}^1$, we set the vectors $A_{\Delta 1} = [0, 0, 0, 1]^T$, $B_{\Delta 1} = [1, 0, 0]^T$ to pick out M_α and Q_M as expressed in (22) and (23). As for the control effectiveness variations, $f_{\Delta 3}^2$, $f_{\Delta 3}^3$ are modeled as parametric uncertainties in pitching moment sensitivity to elevator deflection (represented by M_{δ_e}) and in thrust sensitivity to fuel equivalence ratio (represented by T_ϕ), respectively. Thus, the vectors are set as $A_{\Delta 2} = [0, 0, 0, 1]^T$, $B_{\Delta 2} = [0, 1, 0]^T$ and $A_{\Delta 3} = [0, 0, 1, 0]^T$, $B_{\Delta 3} = [0, 0, 1]^T$.

4. Robust TLC scheme design

In this section, the robust TLC scheme is designed for FAHV. Due to the complexity of the vehicle dynamics, the starting point is to decompose the vehicle dynamics into functional subsystems. Based on the time-scale separation and singular perturbation theory [30,31], the vehicle dynamics are divided into five subsystems, i.e. the velocity, altitude, flight-path angle (FPA), angle of attack (AOA), and pitch rate subsystems. Accordingly, the overall scheme consists of five robust subsystem controllers as depicted in Fig. 5, where the virtual control inputs are drawn as dashed lines. Feedback lines are omitted for simplicity. Fig. 6 shows the structure of each robust controller, which mainly integrates TLC with ESO. TLC contains a pseudo-inversion and a stabilizing controller, constructing a basic control law; ESO estimates the uncertainties to form a

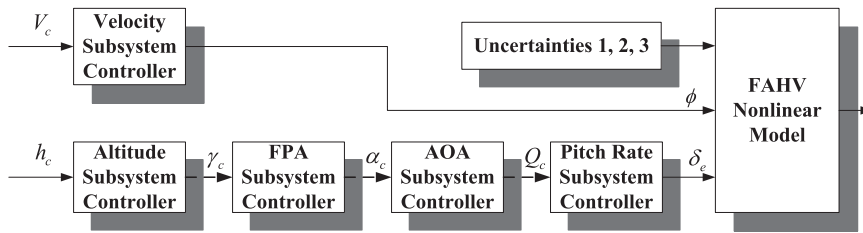


Fig. 5. Overall control scheme.

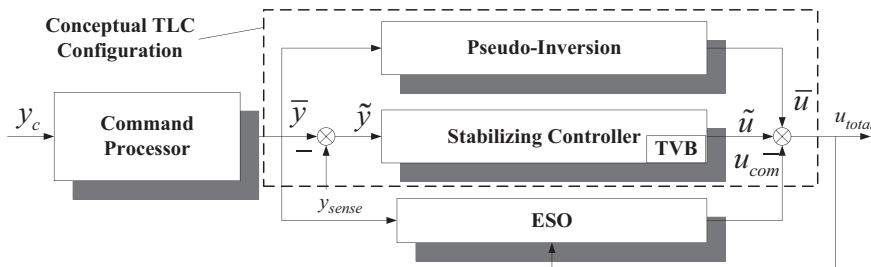


Fig. 6. Structure of each subsystem controller.

compensation control law. In addition, a command processor is added, the effects of which will be addressed later.

4.1. TLC design

Mostly, the control objective is to design a control law that drives the system output to track a nominal output trajectory. In TLC, the original system is firstly linearized along a nominal trajectory, thus the tracking problem is cast into a regulation problem for the error dynamics along the nominal trajectory. Asymptotic tracking can then be achieved by combining a feed-forward pseudo-inversion of the nominal model and a feedback stabilizer of the linearized tracking error dynamics, as shown in the dashed box of Fig. 6. Next, this configuration is adopted to build a basic controller for each subsystem mentioned above.

4.1.1. TLC for the velocity subsystem

In view of the force expressions in (8) and (9), the velocity dynamics (1) can be rewritten as an affine form:

$$\dot{V} = f_V + g_V u_V \quad (24)$$

where

$$f_V = [(\beta_2 \alpha^3 + \beta_4 \alpha^2 + \beta_6 \alpha + \beta_8) \cos \alpha - D]/m - g \sin \gamma$$

$$g_V = (\beta_1 \alpha^3 + \beta_3 \alpha^2 + \beta_5 \alpha + \beta_7) \cos \alpha / m, \quad u_V = \phi$$

Denote the nominal velocity to be tracked as \bar{V} . Replacing V by \bar{V} in f_V and g_V yields \bar{f}_V and \bar{g}_V , respectively. Assume that \bar{g}_V is invertible, which is validated in the whole admissible variable range given in [11]. Then a nominal control law \bar{u}_V can be obtained by the pseudo-inversion:

$$\bar{u}_V = \bar{g}_V^{-1} (\dot{\bar{V}} - \bar{f}_V) \quad (25)$$

here $\dot{\bar{V}}$ is generated by the command processor, which is addressed later.

To design the stabilizing controller, system (24) is first augmented with integral action for disturbance accommodation and performance enhancement. Defining the augmented state $x_V = [\int V dt, V]^T$ and nominal state $\bar{x}_V = [\int \bar{V} dt, \bar{V}]^T$ yields the augmented system

$$\dot{x}_V = [V, f_V]^T + [0, g_V]^T u_V \quad (26)$$

and augmented nominal system

$$\dot{\bar{x}}_V = [\bar{V}, \bar{f}_V]^T + [0, \bar{g}_V]^T \bar{u}_V \quad (27)$$

Define the velocity tracking error as $e_V = x_V - \bar{x}_V$. Then (26) minus (27) yields a tracking error system. Linearizing this tracking error system along the nominal state yields

$$\dot{e}_V = A_V(t)e_V + B_V(t)\tilde{u}_V \quad (28)$$

where

$$A_V(t) = \begin{bmatrix} 0 & 1 \\ 0 & -\rho \bar{V} SC_D / m \end{bmatrix}, \quad B_V(t) = \begin{bmatrix} 0 \\ \bar{g}_V \end{bmatrix}, \quad \tilde{u}_V = u_V - \bar{u}_V$$

Note that modeling error is generated during this linearization procedure because of the nonlinearity of the drag D with respect to V . This modeling error is included in Uncertainty 4. For (28), select a feedback control law as

$$\tilde{u}_V = K_V(t)e_V \quad (29)$$

where $K_V(t) = [k_{V1}(t), k_{V2}(t)]$ are the control gains. Assume the desired closed-loop system matrix $A_{Vc}(t)$ as

$$A_{Vc}(t) = \begin{bmatrix} 0 & 1 \\ -\tau_{V1}(t) & -\tau_{V2}(t) \end{bmatrix}$$

To guarantee the closed-loop stability, LTV PD-spectral theory [29] is adopted to assign the desired dynamics as

$$\begin{cases} \tau_{V1}(t) = \omega_{Vn}^2(t) \\ \tau_{V2}(t) = 2\xi_V \omega_{Vn}(t) - \dot{\omega}_{Vn}(t)/\omega_{Vn}(t) \end{cases} \quad (30)$$

Then according to $A_V + B_V K_V = A_{Vc}$, the control gains are computed as

$$k_{V1}(t) = -\tau_{V1}(t), \quad k_{V2}(t) = -\tau_{V2}(t) + \rho \bar{V} SC_D / m \quad (31)$$

and the feedback control law (29) is obtained.

The total TLC basic control law of the velocity subsystem is

$$u_V = \bar{u}_V + \tilde{u}_V \quad (32)$$

In (30), the constant damping ratio ξ_V and the time-varying bandwidth $\omega_{Vn}(t)$ are the control parameters to be tuned. Particularly, TLC provides such a TVB technique to dynamically assign the closed-loop bandwidth, which can feasibly improve the control performance.

4.1.2. TLC for other subsystems

The control design for the velocity subsystem exhibits a standard TLC design procedure, which can be concluded in six steps: (a) write the original dynamics in an affine form; (b) calculate the pseudo-inversion control law; (c) augment the original dynamics with integral action; (d) linearize the tracking error dynamics along nominal trajectories; (e) assign desired closed-loop dynamics with PD-spectral theory and obtain the stabilizing control law; and (f) add the pseudo-inversion control and the stabilizing control to form the total control law. These six steps can be similarly applied to the other four subsystems. Due to page limitations, the detailed design procedure is omitted here. However, each subsystem has a different affine form. In some cases the affine form may not explicitly exist so that approximation must be made. Therefore, next we will derive all the affine forms for the other four subsystems. Moreover, we will develop an adaptive TVB algorithm.

4.1.2.1. Affine form for the altitude subsystem. Consider the altitude dynamics (3), which can be safely approximated as

$$\dot{h} = V \sin \gamma \approx V \gamma \quad (33)$$

by using the approximation $\sin \gamma \approx \gamma$ which is valid in the whole hypersonic flight. The affine form can be directly obtained as

$$\dot{h} \approx f_h + g_h u_h \quad (34)$$

where

$$f_h = 0, \quad g_h = V, \quad u_h = \gamma$$

Note that the modeling error yielded by the approximation in (33) is included in Uncertainty 4.

4.1.2.2. Affine form for the FPA subsystem. Due to the nonlinear relationship between the thrust and angle of attack in (8) and (9), the FPA dynamics (2) cannot be directly written in an affine form with respect to the virtual control input α . Thus, it is first written in the following form:

$$\dot{\gamma} = f_{\gamma 1} + g_{\gamma 1} \quad (35)$$

where

$$\begin{aligned} f_{\gamma 1} &= \bar{q} S (C_L^{\delta_e} \delta_e + C_L^0) / (mV) - g \cos \gamma / V \\ g_{\gamma 1} &= [\bar{q} S C_L^{\alpha} \alpha + (C_T^{\alpha^3} \alpha^3 + C_T^{\alpha^2} \alpha^2 + C_T^{\alpha} \alpha + C_T^0) \sin \alpha] / (mV) \end{aligned}$$

here $f_{\gamma 1}$ is independent of α , while $g_{\gamma 1}$ is a nonlinear function of α . In order to obtain a linear expression, we utilize the first-order Taylor expansion at the last sampling value α_0 to approximate the nonlinear function $g_{\gamma 1}$. Additionally using $\sin \alpha \approx \alpha$, $g_{\gamma 1}$ is approximated as

$$g_{\gamma 1}(\alpha) \approx g_{\gamma 1}(\alpha_0) + g'_{\gamma 1}(\alpha_0)(\alpha - \alpha_0) = [g_{\gamma 1}(\alpha_0) - g'_{\gamma 1}(\alpha_0)\alpha_0] + g'_{\gamma 1}(\alpha_0)\alpha \quad (36)$$

where

$$\begin{aligned} g_{\gamma 1}(\alpha_0) &= (\bar{q} S C_L^{\alpha} \alpha_0 + C_T^{\alpha^3} \alpha_0^3 + C_T^{\alpha^2} \alpha_0^2 + C_T^{\alpha} \alpha_0 + C_T^0) / (mV) \\ g'_{\gamma 1}(\alpha_0) &= (\bar{q} S C_L^{\alpha} + 4C_T^{\alpha^3} \alpha_0^2 + 3C_T^{\alpha^2} \alpha_0 + 2C_T^{\alpha} + C_T^0) / (mV) \end{aligned}$$

Substituting (36) into (35) produces an affine form as

$$\dot{\gamma} \approx f_{\gamma} + g_{\gamma} u_{\gamma} \quad (37)$$

where

$$f_{\gamma} = f_{\gamma 1} + g_{\gamma 1}(\alpha_0) - g'_{\gamma 1}(\alpha_0)\alpha_0, \quad g_{\gamma} = g'_{\gamma 1}(\alpha_0), \quad u_{\gamma} = \alpha$$

Note that because the Taylor expansion is updated during every sampling period, the approximation is highly reliable. The modeling error is again included in Uncertainty 4.

4.1.2.3. Affine form for the AOA subsystem. The angle of attack dynamics can be easily written in an affine form by taking (2) into (4):

$$\dot{\alpha} = f_{\alpha} + g_{\alpha} u_{\alpha} \quad (38)$$

where

$$f_{\alpha} = -(L + T \sin \alpha) / (mV) + g \cos \gamma / V, \quad g_{\alpha} = 1, \quad u_{\alpha} = Q$$

4.1.2.4. Affine form for the pitch rate subsystem. With the pitching moment expression in (8) and (9), the pitch rate dynamics (5) is cast into the affine form

$$\dot{Q} = f_Q + g_Q u_Q \quad (39)$$

where

$$\begin{aligned} f_Q &= (z_T T + \bar{q} S C_{M,\alpha} + \tilde{\psi}_f \ddot{\eta}_f + \tilde{\psi}_a \ddot{\eta}_a) / I_{yy}, \\ g_Q &= \bar{q} S C_{M,e} / I_{yy}, \quad u_Q = \delta_e \end{aligned}$$

Note that the flexible modes exist in f_Q , resulting in strong coupling effects to rigid body dynamics. We design a pitch rate subsystem controller that directly considers these elastic deformations, so these coupling effects can be well suppressed. Another way is to take the flexible effects as disturbances, as done in [11].

4.1.3. Adaptive TVB algorithm

As stated in Section 3.2, the dynamic pressure \bar{q} has a great impact on the vehicle characteristics. In large velocity or altitude maneuvers, \bar{q} shows a fast time-varying feature. Linearization of the vehicle model at trim conditions [8] indicates that the following approximate relationship holds between the dynamic pressure and the natural frequency $\omega_{pn}(t)$ of the phugoid mode:

$$\omega_{pn}^2(t) \propto \bar{q} \quad (40)$$

Therefore, to enhance the system robustness and tracking performance, we design an adaptive TVB algorithm as

$$\omega_{pn}(t) = \omega_{pn0} \sqrt{\bar{q} / \bar{q}_0} \quad (41)$$

where ω_{pn0} and \bar{q}_0 are the bandwidth and dynamic pressure at an initial trim condition, respectively. The physical interpretation of (41) lies in the fact that with an increasing dynamic pressure all forces and moments increase, which makes all flight dynamics change faster, thus the relevant bandwidth should be increased and vice versa. Simulation indicates that the above TVB algorithm can also be applied to short period and altitude modes. Additionally, later the stability analysis in Section 5 will show that this algorithm can suppress a larger disturbance and yield a smaller tracking error.

As shown in Fig. 3, \bar{q} significantly affects the rotational dynamics. Thus this adaptive TVB algorithm is primarily applied to the angle of attack and pitch rate subsystems.

4.2. Extended state observer design

Perturbation analysis shows that the basic TLC frame can guarantee local exponential stability only when perturbation is limited in a certain range [22]. To enhance the system robustness, nonlinear ESO [26–28] is integrated with the basic TLC frame. The core idea of ESO is to take all internal and external uncertainties modeled in Section 3.5 as a new extended state, and then establish a state observer to estimate these uncertainties.

Still take the velocity subsystem for demonstration. Assume the disturbed velocity dynamics as

$$\dot{V} = f_V + g_V u_V + \Delta_V \quad (42)$$

with Δ_V denoting the total uncertainty. Let $x_{V1} = V$, $x_{V2} = \Delta_V$, where x_{V2} is an extended state. Suppose that $\dot{\Delta}_V = -w_V(t)$ with $w_V(t)$ unknown but bounded. Then (42) can be written as a second-order extended system:

$$\dot{x}_{V1} = f_V + g_V u_V + x_{V2}, \quad \dot{x}_{V2} = -w_V(t) \quad (43)$$

An ESO is established for (43) as

$$\begin{cases} \dot{\tilde{z}}_V = z_{V1} - x_{V1} \\ \dot{\tilde{z}}_{V1} = f_V + g_V u_V + z_{V2} - \beta_{V1} \tilde{z}_V \\ \dot{\tilde{z}}_{V2} = -\beta_{V2} fal(\tilde{z}_V, \alpha_V, \delta_V) \end{cases} \quad (44)$$

where \tilde{z}_V denotes the estimation error of the output variable, z_{Vi} is the estimation value of x_{Vi} , and β_{Vi} is the estimation gain, $i = 1, 2$. fal is a nonlinear function of \tilde{z}_V , expressed as [28]

$$fal(\tilde{z}_V, \alpha_V, \delta_V) = \begin{cases} |\tilde{z}_V|^{\alpha_V} \text{sign}(\tilde{z}_V), & |\tilde{z}_V| > \delta_V \\ \tilde{z}_V / \delta_V^{1-\alpha_V}, & |\tilde{z}_V| \leq \delta_V \end{cases} \quad (45)$$

where δ_V, α_V are constants with $\delta_V > 0$ and $0 < \alpha_V < 1$. The meanings of these parameters can be found in [28]. By properly choosing the parameters $\beta_{V1}, \beta_{V2}, \alpha_V$, and δ_V , we have $z_{V1} \rightarrow V, z_{V2} \rightarrow \Delta_V$. Here the gains β_{V1} and β_{V2} may affect the estimation dynamic process. Redefine estimation errors as $e_{V1} = z_{V1} - V, e_{V2} = z_{V2} - \Delta_V$. For a constant disturbance ($w_V(t) = 0$), the phase portraits of the estimation error dynamics with the same initial values but four different groups of estimation gains are depicted in Fig. 7. All solution trajectories converge to (0, 0), indicating that ESO can perfectly estimate both the original state and the extended state (the disturbance). However, the estimation dynamic processes in these four cases are quite different. Considering both the rapidity and the overshoot, we choose $\beta_{V1} = \beta_{V2} = 15$ in the final robust scheme.

The estimation value z_{V2} can then be applied to obtain a compensation control law as

$$u_{Vcom} = g_V^{-1} z_{V2} \quad (46)$$

This together with the basic TLC control law (32) produces the final robust control law for the velocity subsystem:

$$u_V = \bar{u}_V + \tilde{u}_V - u_{Vcom} \quad (47)$$

4.3. Command processor design

As shown in Fig. 6, the control command needs to pass through a command processor. It has two functions: to cast the original command into one that is more realizable and to generate the derivative of the nominal trajectory used in the pseudo-inversion. In this work, it is implemented by the arranged transient process (ATP) technique [26–28], which is expressed in the following discrete-time form:

$$\begin{cases} \vartheta_1(k+1) = \vartheta_1(k) + \tau \vartheta_2(k) \\ \vartheta_2(k+1) = \vartheta_2(k) + \tau fhan(\vartheta_1(k) - \vartheta(k), \vartheta_2(k), r_\vartheta, \tau) \end{cases} \quad (48)$$

where τ stands for the sampling period, ϑ is the original command, while ϑ_1 and ϑ_2 are the arranged process and its derivative with initial values $\vartheta_1(0) = \vartheta(0), \vartheta_2(0) = 0$. Here, the function $fhan$ is the time-optimal control law for a discrete double integral system and its expression can be found in [28]. r_ϑ is the only parameter to be tuned. Compared with the so-called “prefilter” which is widely applied such as in [8–12,14], ATP uses only one parameter r_ϑ to feasibly arrange the desired transient time according to

$$T_0 = \sqrt{4c/r_\vartheta} \quad (49)$$

where c is the original step value and T_0 is the transient time.

5. Stability analysis

In this section, the stability of the overall closed-loop system (consisting of five interconnected subsystems) with the robust TLC scheme is analyzed. Although the PD-spectral theory can guarantee the stability of the linearized tracking-error dynamics (28) (for the velocity subsystem, for example), three additional issues need to be considered for the stability analysis of the overall closed-loop system: (a) Uncertainty 4 generated during the mathematical derivation procedure of

TLC; (b) Uncertainties 1, 2, and 3, since ESO is applied to estimate these uncertainties, the stability of nonlinear ESO and the estimation error need to be further considered; and (c) the singular perturbation effects among the five interconnected subsystems. Overall analysis involves PD-eigenvalue assignment and stability theories of systems with regular and singular perturbations, which is beyond the focus of this paper. Therefore, we only present the main analysis results and an outline of the proof here. The analysis offers us guidelines to design the TVB algorithm in real-time. In the following analysis, we first investigate the stability of each single subsystem with Uncertainties 1–4. The nonlinear ESO stability and estimation error are analyzed. Based on the analysis results for each subsystem, the stability of the overall closed-loop system with singular perturbations is discussed at last.

Still take the velocity subsystem for demonstration. The closed-loop disturbed system with integration augmentation can be rewritten as

$$\dot{x}_V = [V, f_V]^T + [0, g_V]^T u_V + [0, \Delta_V]^T \quad (50)$$

where $x_V = [\int V dt, V]^T, f_V$ and g_V are given in (24), and the robust control law u_V is given in (47). Defining nominal state $\bar{x}_V = [\int \bar{V} dt, \bar{V}]^T$ produces the augmented nominal system (27). Then (50) minus (27) yields the closed-loop tracking error system as

$$\begin{aligned} \dot{e}_V &= \dot{x}_V - \dot{\bar{x}}_V = [V - \bar{V}, f_V + g_V(\bar{u}_V + \tilde{u}_V - u_{Vcom}) \\ &\quad + \Delta_V - (\bar{f}_V + \bar{g}_V \bar{u}_V)]^T \\ &= [V - \bar{V}, f_V + g_V(\bar{u}_V + \tilde{u}_V) - (\bar{f}_V + \bar{g}_V \bar{u}_V)]^T + [0, e_\Delta]^T \end{aligned} \quad (51)$$

where $e_\Delta = \Delta_V - g_V u_{Vcom} = \Delta_V - z_{V2}$ is the uncertainty estimation error of the velocity subsystem. As done in Section 4.1.1, linearizing the undisturbed system along nominal states and control inputs yields the linearized tracking error system (28), then the stabilizing control law is obtained in (29). During this procedure, however, linearization error is produced, denoted as $m(t, e_V)$. So (51) can be written as the sum of a LTV part, a modeling error part, and an uncertainty estimation error part

$$\begin{aligned} \dot{e}_V &= [A_V(t) + B_V(t)K_V(t)]e_V + m(t, e_V) + [0, e_\Delta]^T \\ &= \underbrace{A_V(t)e_V}_{\text{LTV part}} + \underbrace{m(t, e_V)}_{\text{modeling error part}} + \underbrace{[0, e_\Delta]^T}_{\text{uncertainty estimation error part}} \end{aligned} \quad (52)$$

where $m(t, e_V)$ is defined as

$$m(t, e_V) = [V - \bar{V}, f_V + g_V(\bar{u}_V + \tilde{u}_V) - (\bar{f}_V + \bar{g}_V \bar{u}_V)]^T - A_V(t)e_V$$

With the PD-spectral theory, $K_V(t)$ is chosen such that the LTV tracking error dynamics

$$\dot{e}_V = A_V(t)e_V \quad (53)$$

is exponentially stable. The following theorem indicates that under some bounded modeling error $m(t, e_V)$ and bounded estimation error e_Δ , the tracking error e_V in (52) is bounded.

Theorem 1. [22] For the nonlinear tracking error dynamics (52), suppose that $e_V \in \mathcal{R}^n$ and

- (i) $K_V(t)$ is designed following the standard TLC procedure such that the closed-loop linearized tracking error system

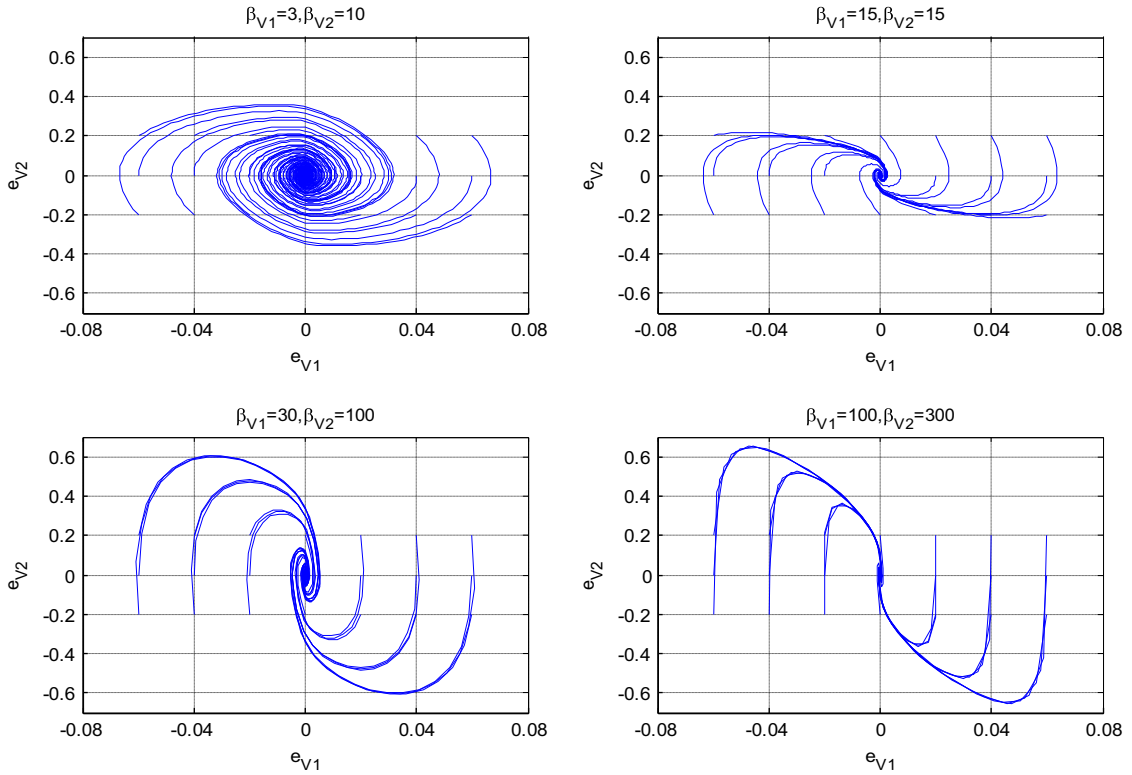


Fig. 7. Phase portraits of the estimation error dynamics with different gains.

(53) is exponentially stable. $A_{Vc}(t)$ has the finite and smooth PD-spectrum $\{\rho_i(t)\}_{i=1}^n$, which satisfies

$$\sup(\operatorname{Re}\rho_i(t)) = -m_i, \quad \sup|\rho_i(t)| = M$$

where m_i and M are positive constants and $\operatorname{Re}\rho_i(t)$ is the real part of the time-varying eigenvalue $\rho_i(t)$.

- (ii) For a given positive constant L_2 , there exists a positive constant r such that the modeling error satisfies

$$\|m(t, e_V)\| \leq L_2 \|e_V\|^2$$

in $[0, \infty) \times \mathfrak{V}$ and $\mathfrak{V} = \{e_V \in \mathbb{R}^n \mid \|e_V\| < r\}$.

- (iii) The uncertainty estimation error e_Δ satisfies

$$\|e_\Delta\| \leq \delta_f = \frac{\theta_1 \theta_2 c_3 \nu_1}{c_4 k_1^3} \sqrt{\frac{c_3 \nu_1}{c_4 L_1}} \sigma$$

for some constants $0 < \theta_1 < 1$, $0 < \theta_2 < 1$, $0 < c_3 \leq c_4$, $k_1 > 0$, $L_1 > 0$, and $\nu_1 > 0$.

Then, there exists positive constant bound $b > 0$ such that for

$$\|e_V(t_0)\| < \sqrt{\frac{c_3 \nu_1}{c_4 L_1}} \frac{\sigma}{k_1}$$

the solution of (52) satisfies

$$\begin{cases} \|e_V\| \leq k_2 \exp(-\nu_2(t-t_0)) \|e_V(t_0)\|, & \forall t_0 \leq t < t_1 \\ \|e_V\| \leq b, & \forall t \geq t_1 \end{cases}$$

for some finite time t_1 , where

$$\begin{aligned} \nu_2 &= \nu_1 \frac{(1-\theta_2)\theta_1 c_3}{k_1^2 c_4}, & k_2 &= k_1 \sqrt{\frac{c_4 L_1}{c_3 \nu_1}}, \\ b &= \frac{k_1^3 c_4 \delta_f}{\nu_1 c_3 \theta_1 \theta_2} \sqrt{\frac{c_4 L_1}{c_3 \nu_1}}, & \sigma &= \min \left\{ r, \frac{(1-\theta_1)c_3 \nu_1}{k_1^2 c_4 L_2} \right\}. \end{aligned}$$

The proof of Theorem 1 is omitted here and was given in [22], which utilized the PD-eigenvalue assignment and the stability theory of regular perturbed system (Lemma 9.2, [32]). σ is the tracking error bound for (52) when $e_\Delta = 0$, while b is the tracking error bound when $e_\Delta \neq 0$, $e_\Delta \leq \delta_f$ where δ_f is the uncertainty estimation error bound. The independent parameters above include $\{\theta_1, \theta_2, c_3, c_4, r, L_2, L_1, k_1, \nu_1\}$, where $\theta_1, \theta_2, c_3, c_4$ are related to the Lyapunov function for stability analysis of (53), r, L_2 describe the condition that the linearization error should obey, and L_1, k_1, ν_1 are closely related to the PD-eigenvalue assignment defined as

$$L_1 = \sup \|A_{Vc}(t)\|_2, \quad \nu_1 = \min \{m_i\}, \quad \|\Phi_V(t, \tau)\| \leq k_1 \exp(-\nu_1(t-\tau)) \quad (54)$$

here $\|\cdot\|_2$ is the induced 2-norm, and $\Phi_V(t, \tau)$ is the transition matrix for (53). Physically, ν_1 corresponds to the slowest convergence rate of (53). In view of the expressions of b and δ_f , if ν_1 is increased by a TVB algorithm such as (41), the ultimate tracking error bound is decreased and the

uncertainty estimation error bound is increased, thus the system robustness is enhanced. This offers a guide to design a TVB algorithm.

Theorem 1 requires that the uncertainty estimation error e_d is bounded. This involves the stability analysis of nonlinear ESO. For this problem, Han et al. obtained some sufficient conditions to guarantee the stability via two methods: the Lyapunov method [33] and the self-stable region approach [34]. Subsequently, the estimation error bound can be obtained. In this work, we present another different method to investigate the nonlinear ESO stability where the ESO estimation error dynamics is treated as a generalized Liénard system with forcing item [35,36]. New results are obtained, particularly on the asymptotic behavior of the estimation error when derivatives of the uncertainties are absolutely integrable. Consider the extended system (43) and its ESO (44). Redefine the estimation errors as $e_{V1} = z_{V1} - x_{V1}$, $e_{V2} = z_{V2} - x_{V2}$. An equivalent system can be constructed as

$$\begin{cases} \dot{z}_1 = z_2 \\ \dot{z}_2 = -\beta_{V1}z_2 - \beta_{V2}f\alpha(z_1, \alpha_V, \delta_V) + w_V(t) \end{cases} \quad (55)$$

where z_1 and z_2 are defined as $z_1 = e_{V1}$, $z_2 = e_{V2} - \beta_{V1}e_{V1}$. Without loss of generality, write (55) in a general form as

$$\begin{cases} \dot{z}_1 = z_2 \\ \dot{z}_2 = -f(z_1)z_2 - g(z_1) + w(t) \end{cases} \quad (56)$$

This is a standard form of generalized Liénard system with forcing item $w(t)$. We have the following asymptotic stability theorem.

Theorem 2. For system (56), suppose that

- (i) $f(z_1)$, $g(z_1)$ and $w(t)$ are continuous;
- (ii) $z_1g(z_1) > 0$ ($z_1 \neq 0$), $g(0) = 0$;
- (iii) $f(z_1) > 0$ and $F(z_1) = \int_0^{z_1} f(u)du \rightarrow \pm\infty$ as $z_1 \rightarrow \pm\infty$;
- and
- (iv) $W(t) = \int_0^t |w(s)|ds < \infty$.

Then all solutions of (56) satisfy $z_1 \rightarrow 0$, $z_2 \rightarrow 0$ as $t \rightarrow \infty$.

The proof needs Theorem 8.8 and Theorem 10.3 in [35]. Due to page limitations, these two theorems are not given here, but separately denoted correspondingly as Lemma 1 and Lemma 2. Then we use them to prove Theorem 2.

Proof. According to Lemma 1, the solutions of (56) are uniformly bounded. Construct a continuous function as

$$V(t; z_1, z_2) = e^{-2W(t)}[G(z_1) + z_2^2/2 + 1]$$

where

$$G(z_1) = \int_0^{z_1} g(u)du \geq 0$$

we have

$$V(t; z_1, z_2) \geq e^{-2E(\infty)}z_2^2/2 \geq 0$$

and

$$\begin{aligned} \dot{V} &= e^{-2W(t)}\{-2|w(t)|(G(z_1) + z_2^2/2 + 1) + g(z_1)z_2 \\ &\quad - f(z_1)z_2^2 - g(z_1)z_2 + z_2w(t)\} \end{aligned}$$

$$\begin{aligned} &\leq e^{-2W(t)}\{-|w(t)|(z_2^2 + 2 - |z_2^2|) - f(z_1)z_2^2\} \\ &= e^{-2W(t)}\{-|w(t)|[(|z_2| - 1/2)^2 + 7/4] - f(z_1)z_2^2\} \\ &\leq -f(z_1)z_2^2e^{-2W(t)} \leq -f(z_1)z_2^2e^{-2W(\infty)} \end{aligned}$$

Define

$$W(z_1, z_2) = f(z_1)z_2^2e^{-2W(\infty)}$$

then $W(z_1, z_2)$ is a positive definite function with respect to the set $\Omega_z = \{(z_1, z_2) | z_2 = 0\}$. According to Lemma 2, all solutions of (56) approach Ω_z . Moreover, in view of the system form in Lemma 2, we rewrite (56) as

$$\dot{z} = F_z(t, z) + G_z(t, z),$$

where

$$z = \begin{bmatrix} z_1 \\ z_2 \end{bmatrix}, \quad F_z(t, z) = \begin{bmatrix} z_2 \\ -f(z_1)z_2 - g(z_1) \end{bmatrix}, \quad G_z(t, z) = \begin{bmatrix} 0 \\ w(t) \end{bmatrix}$$

For $(z_1, z_2) \in \Omega_z$, as $t \rightarrow \infty$, we have

$$F(t, z) \rightarrow \begin{bmatrix} 0 \\ -g(z_1) \end{bmatrix}$$

According to Lemma 2, every solution of (56) approaches the largest semi-invariant set of the system

$$\begin{cases} \dot{z}_1 = 0 \\ \dot{z}_2 = -g(z_1) \end{cases}$$

By the condition on $g(z_1)$, the largest semi-invariant set contained in Ω_z is only the origin. Therefore, we conclude that $z_1 \rightarrow 0$, $z_2 \rightarrow 0$ as $t \rightarrow \infty$. \square

Since $z_1 \rightarrow 0$, $z_2 \rightarrow 0$, the estimation errors e_{V1}, e_{V2} are bounded. So this theorem indicates that, for uncertainties that own absolutely integrable derivatives, if the nonlinear ESO is designed as illustrated in (44) and (45), the ultimate estimation errors will be bounded.

Now that the stability behaviors of nonlinear ESO and each subsystem are, respectively, described in Theorems 2 and 1, the final issue is to investigate the stability of the overall system that includes the five interconnected subsystems. Singular perturbations need to be considered. A detailed discussion was given in [23], which primarily relied on the PD-spectral theory and the stability theory in [32] (Theorem 11.4). The main conclusion is that, if the boundary-layer system (fast-state system) is exponentially stable (guaranteed by Theorem 1), and the linearized tracking error dynamics of the reduced order system (slow-state system) can be stabilized by PD-eigenvalue assignment, then the overall system is exponentially stable for the time-scale ratio $\varepsilon < \varepsilon^*$. Here ε^* is the time-scale ratio bound, which is related to the PD-eigenvalue parameter ν_1 (defined in (54)). For a given time-scale ratio ε , if ν_1 is increased by a TVB algorithm such as (41), ε^* can be increased. Subsequently, the system robustness to singular perturbations is enhanced. A guide to introduce the singular perturbation and time-scale separation theory into aerospace systems can be found in [30,31].

6. Simulations

To illustrate the effectiveness of the proposed robust TLC scheme, two representative flight cases for FAHV are

studied: a climbing maneuver at constant dynamic pressure (Case 1) and a climbing maneuver with longitudinal acceleration using separate reference commands for altitude and velocity (Case 2). The initial trim condition is listed in Table 3. Parameters for ATP and TLC are given in Table 4. Parameters for ESO are all set as $\beta_{i1} = \beta_{i2} = 15$, $\alpha_i = 0.5$, $\delta_i = 0.01$, $i = V, h, \gamma, \alpha, Q$, which shows a great parameter adaption property.

Table 3
Initial trim condition.

State	Value	State	Value	State	Value	Input	Value
V	7700 ft/s	α	1.5153°	$\dot{\eta}_f$	0	δ_e	11.4635°
h	85,000 ft	Q	0°/s	η_a	1.2114	ϕ	0.2514
γ	0°	η_f	1.5122	$\dot{\eta}_a$	0		

Table 4
Control parameters.

Parameter	Value	Parameter	Value	Parameter	Value
r_V	0.15	ω_V	0.02	ξ_V	0.7
r_h	1	ω_h	0.02	ξ_h	0.7
r_γ	0.001	ω_γ	0.05	ξ_γ	1
r_α	0.05	ω_α	0.25	ξ_α	0.7
r_Q	0.5	ω_Q	1	ξ_Q	0.7

In Case 1, the altitude command is given to let the vehicle climb from 85,000 ft to 95,000 ft, whereas the velocity command is generated by solving the air density model to maintain constant dynamic pressure at 2000 psf. When no uncertainty is added, robust tracking results are depicted in Fig. 8. Both the outputs and the internal states are tracked well. Note that the response of the altitude exhibits a typical undershoot behavior due to the non-minimum phase feature as already analyzed. As a general rule, the control inputs increase in the first half of transient time while decreasing in the second half. This is due to the ATP feature which accelerates the arranged transient process in the first half of transient time while decelerating it in the second half.

To make the test more demanding, uncertainties are added next. First, air density variations are verified in the robust TLC scheme. -40% , 0% , and $+40\%$ of air density uncertainties are separately considered, yielding the simulation results depicted in Fig. 9. It is seen that the commanded velocity and altitude are tracked well under all these three conditions, indicating a good uncertainty rejection ability of the robust TLC scheme. In addition, increased air density leads to increased control effectiveness for both the elevator and the engine system, thus the tracking performances are improved, see Fig. 9a and b. Accordingly, the required angle of attack and elevator deflection angle are decreased, see Fig. 9c and e. In contrast, the required fuel equivalence ratio is increased due to the decrease of the angle of attack (Fig. 9f), indicating a strong coupling between the aerodynamics and the engine system.

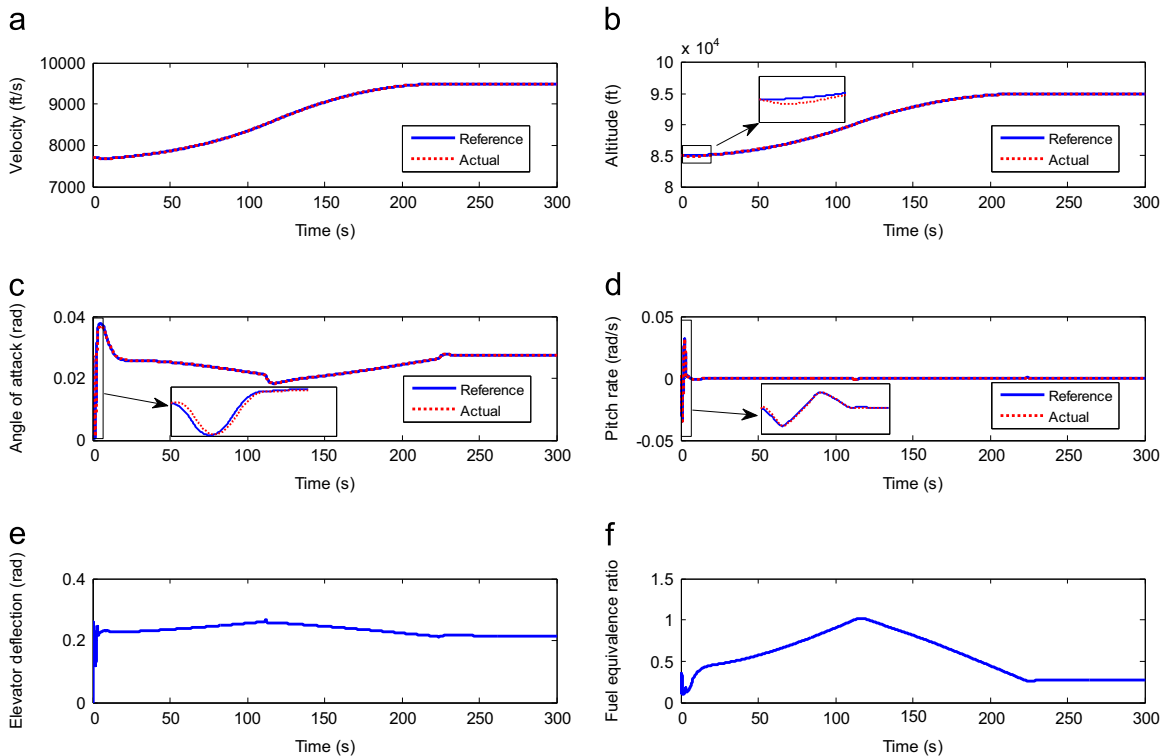


Fig. 8. Tracking results and the control inputs with no uncertainty in the robust TLC scheme.

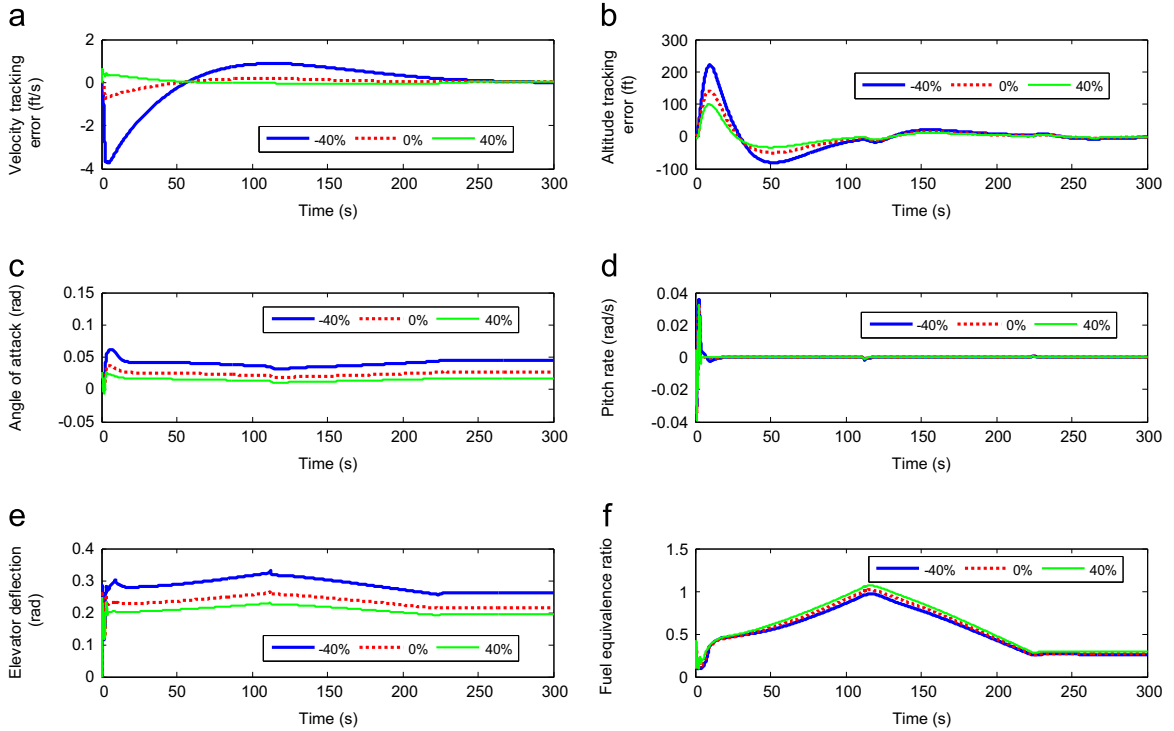


Fig. 9. Responses under air density uncertainty in the robust TLC scheme.

Next, effects of strong instant airflows modeled as (17) are verified. The pitching moment disturbance is set as

$$\Delta f_q = \begin{cases} (10^6 + 10^5 \sin(40\pi t))/I_{yy}, & 50 \leq t \leq 55 \text{ s} \\ -(10^6 + 10^5 \sin(40\pi t))/I_{yy}, & 250 \leq t \leq 255 \text{ s} \\ 0, & \text{other time} \end{cases} \quad (57)$$

This disturbance includes pulse perturbations with large amplitude (10^6 lbf ft) and sine wave perturbations with high frequency (20 Hz). It is activated in two stages to separately verify the disturbance influences during the transient process and the steady-state process. For comparison purposes, we denote the control scheme that includes TCL without ESO compensation as a basic TLC frame, differing from the robust TLC scheme. Comparison simulation results are shown in Fig. 10. In the basic frame, shown as the dotted lines in Fig. 10 (a)–(d), oscillation occurs in the output and control input responses due to the airflow disturbance. On the contrary, this disturbance is suppressed in the robust scheme by ESO compensation, shown as the solid lines in Fig. 10(a)–(d). The disturbed pitching moment is shown in Fig. 10(e). The true and estimated values of the disturbance are shown in Fig. 10 (f). It is seen that ESO can estimate the disturbance with a high accuracy; in addition, it also behaves as a low-pass filter to suppress the high frequency component of the disturbance.

In the next simulation, multiple uncertainties are simultaneously added. First consider a small uncertainty case: 25% of flexibility uncertainties, 40% of variations in thrust control effectiveness, and wind gust uncertainty merely in the velocity dynamics (setting $f_{\Delta 2}^3(x, u, t) = [2 \sin t, 0, 0, 0, 0]^T$). In this case both the basic TLC

frame and the robust TLC scheme provide stable tracking results, as shown in Fig. 11a and b, but the basic TLC frame exhibits a large oscillation in the velocity response. Next, 40% of propulsive perturbations and 40% of variations in elevator control effectiveness are also added, and the wind gusts in (16) are included. For this large uncertainty case, the robust scheme still performs well, as shown in Fig. 11c and d. However, the basic TLC frame completely loses its control ability and the responses diverge quickly (thus the tracking figures are omitted here). In the robust scheme, the true and estimated values of uncertainties in the velocity and pitch rate dynamics are given in Fig. 11e and f, where the excellent estimation ability of ESO is exhibited.

Case 2 conducts a more aggressive maneuver where the velocity and altitude commands are independently given as 1000 ft/s and 12,000 ft, respectively. All uncertainties considered in Case 1 are included. Tracking results in the basic TLC frame are omitted because all responses diverge quickly, while tracking results in the robust scheme are depicted in Fig. 12. Although the dynamic pressure experiences a slightly large decrease, which may significantly affect the vehicle characteristics, the velocity and altitude tracking results still remain excellent. The internal states such as the angle of attack chatter due to the uncertainties, but they all stay in admissible ranges.

7. Conclusions

Robust control design is a fundamental issue for FAHV with multiple uncertainties. In this work, comprehensive uncertainties resulting from flexibility, aerodynamic

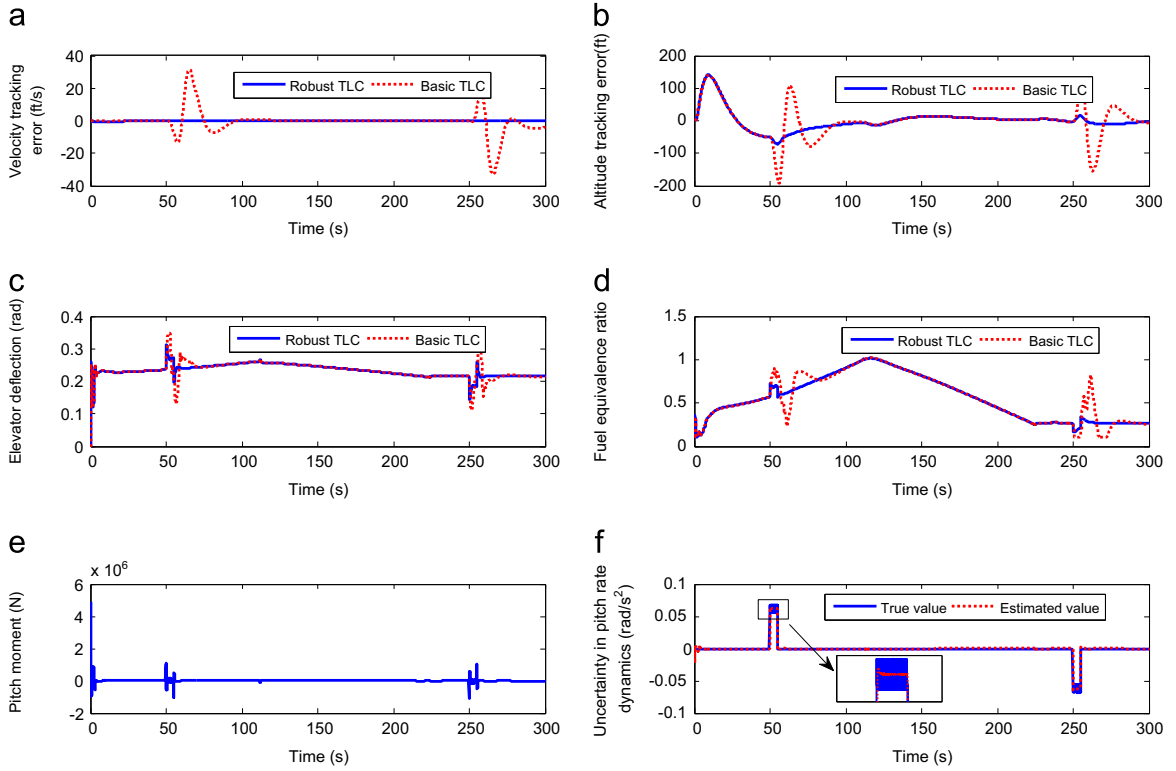


Fig. 10. Comparison responses under strong instant airflows.

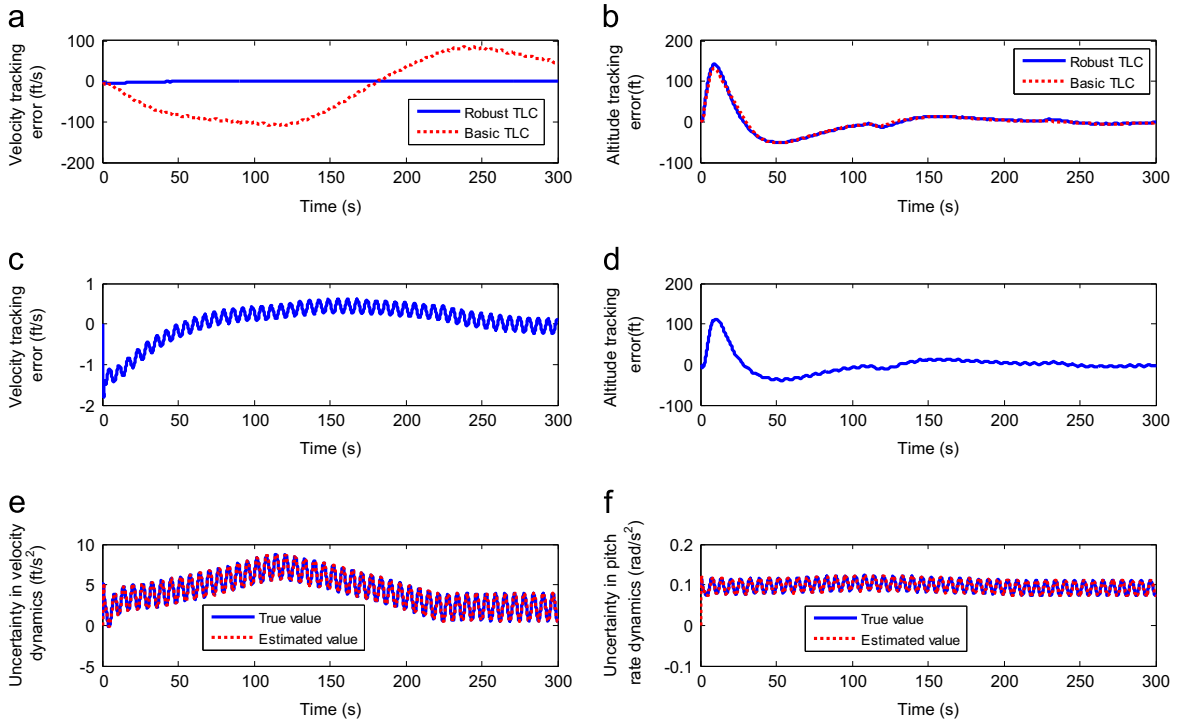


Fig. 11. Comparison responses under multiple uncertainties.

parameter variations, environmental disturbances, and control-oriented modeling errors are analyzed, offering a better understanding of the complex vehicle features.

A uniform nonlinear uncertainty model is developed, which lumps the first three uncertainties together and therefore is beneficial for compensation law design and closed-loop

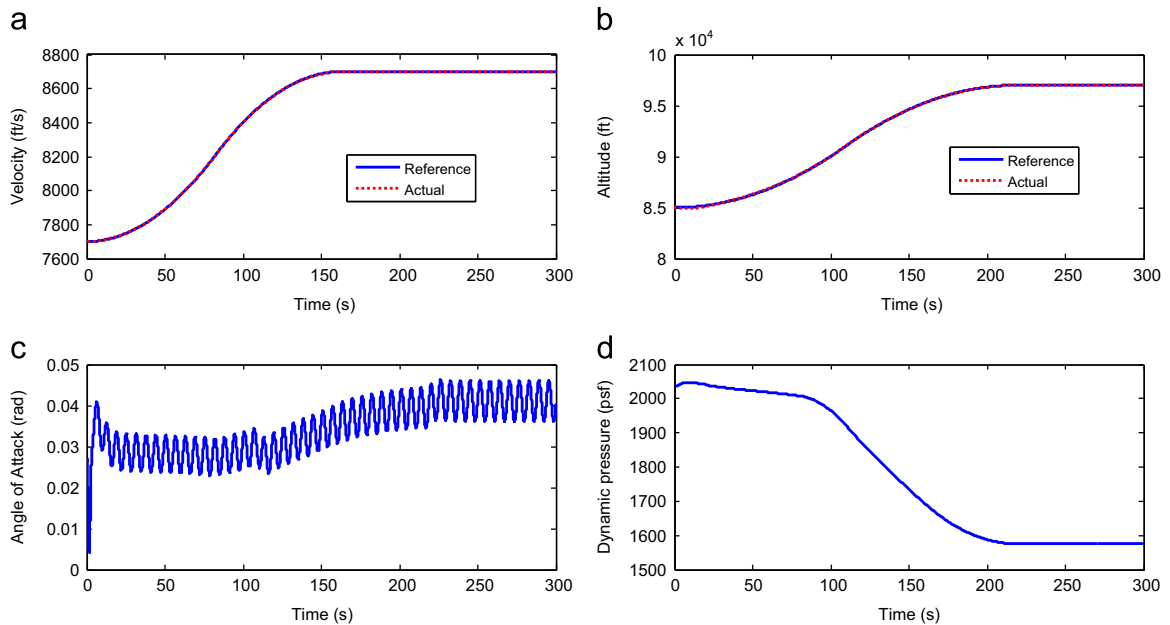


Fig. 12. Tracking results with mixed uncertainties in the robust TLC scheme for Case 2.

stability analysis. For control design, the vehicle dynamics are decomposed into five functional subsystems based on time-scale separation and singular perturbation theory. Then a robust control scheme is proposed, which consists of five subsystem controllers, each for a subsystem. This robust scheme is based on the TLC method and the ESO technique, where TLC can guarantee the exponential stability of each subsystem along nominal flight trajectories, and ESO can estimate the uncertainties with high efficiency. The stability of the overall closed-loop system is analyzed, where the four aforementioned uncertainties and additional singular perturbations among the five subsystems are considered. Comparison simulation demonstrates the great tracking performance and the uncertainty rejection ability of the proposed robust scheme.

Acknowledgment

This work was partly supported by the National Natural Science Foundation of China (Grants nos. 61273149, 61203003, and 61273336) and the Special Project for Innovation Methods of MOST (Grant no. 2012IM010200).

References

- [1] R.T. Volland, L.D. Huebner, C.R. McClinton, X-43A Hypersonic vehicle technology development, *Acta Astronautica* 59 (1–5) (2006) 181–191.
- [2] Factsheets: X-51A waverider, U.S. Air Force (<http://www.af.mil/Information/factsheets/factsheet.asp?fsID=17986>), 3 May 2013 (accessed 09.05.13).
- [3] M.A. Bolender, D.B. Doman, A non-linear model for the longitudinal dynamics of a hypersonic air-breathing vehicle, in: Proceedings of the AIAA Guidance, Navigation and Control Conference and Exhibit, AIAA 2005-6255, 2005.
- [4] M.A. Bolender, D.B. Doman, Nonlinear longitudinal dynamical model of an air-breathing hypersonic vehicle, *J. Spacecr. Rockets* 44 (2) (2007) 374–387.
- [5] M. Mirmirani, C. Wu, A. Clark, S. Choi, R. Colgren, Modeling for control of a generic airbreathing hypersonic vehicle, in: Proceedings of the AIAA Guidance, Navigation and Control Conference and Exhibit, AIAA 2005-6256, 2005.
- [6] M.A. Bolender, D.B. Doman, Flight path angle dynamics of airbreathing hypersonic vehicles, in: Proceedings of the AIAA Guidance, Navigation and Control Conference and Exhibit, AIAA 2006-6692, 2006.
- [7] T. Williams, M.A. Bolender, D.B. Doman, O. Morataya, An aerothermal flexible mode analysis of a hypersonic vehicle, in: Proceedings of the AIAA Guidance, Navigation and Control Conference and Exhibit, AIAA 2006-6647, 2006.
- [8] D.O. Sighthorsson, P. Jankovsky, A. Serrani, S. Yurkovich, M.A. Bolender, D.B. Doman, Robust linear output feedback control of an airbreathing hypersonic vehicle, *J. Guid., Control, Dyn.* 29 (2) (2008) 1052–1066.
- [9] Z.D. Wilcox, W. MacKunis, S. Bhat, R. Lind, W.E. Dixon, Lyapunov-based exponential tracking control of a hypersonic aircraft with aerothermoelastic effects, *J. Guid., Control, Dyn.* 33 (4) (2010) 1213–1224.
- [10] X.X. Hu, L.G. Wu, C.H. Hu, H.J. Gao, Adaptive sliding mode tracking control for a flexible air-breathing hypersonic vehicle, *J. Franklin Inst.* 349 (2) (2012) 559–577.
- [11] J.T. Parker, A. Serrani, S. Yurkovich, M.A. Bolender, D.B. Doman, Control-oriented modeling of an air-breathing hypersonic vehicle, *J. Guid., Control, Dyn.* 30 (3) (2007) 856–869.
- [12] L. Fiorentini, A. Serrani, M.A. Bolender, D.B. Doman, Nonlinear robust adaptive control of flexible air-breathing hypersonic vehicles, *J. Guid., Control, Dyn.* 32 (2) (2009) 401–416.
- [13] Q. Zong, J. Wang, B.L. Tian, Y. Tao, Quasi-continuous high-order sliding mode controller and observer design for flexible hypersonic vehicle, *Aerosp. Sci. Technol.* 27 (1) (2013) 127–137.
- [14] O. Rehman, B. Fidan, I. Petersen, Uncertainty modeling and robust minimax LQR control of hypersonic flight vehicles, in: Proceedings of the AIAA Guidance, Navigation and Control Conference and Exhibit, AIAA 2010-8285, 2010.
- [15] H. Buschek, A.J. Calise, Uncertainty modeling and fixed-order controller design for a hypersonic vehicle model, *J. Guid., Control, Dyn.* 20 (1) (1997) 42–48.
- [16] F.R. Chavez, D.K. Schmidt, Uncertainty modeling for multivariable-control robustness analysis of elastic high-speed vehicles, *J. Guid., Control, Dyn.* 22 (1) (1999) 87–95.
- [17] M. Kuipers, M. Mirmirani, P. Ioannou, Y. Huo, Adaptive control of an aeroelastic airbreathing hypersonic cruise vehicle, in: Proceedings of the AIAA Guidance, Navigation and Control Conference and Exhibit, AIAA 2007-6326, 2007.
- [18] J. Levin, P. Ioannou, M. Mirmirani, Adaptive mode suppression scheme for an aeroelastic airbreathing hypersonic cruise vehicle,

- in: Proceedings of the AIAA Guidance, Navigation and Control Conference and Exhibit, AIAA 2008-7137, 2008.
- [19] J.J. Zhu, B.D. Banker, C.E. Hall, X-33 ascent flight control design by trajectory linearization – a singular perturbation approach, in: Proceedings of the AIAA Guidance, Navigation, and Control Conference and Exhibit, AIAA 2000-4159, 2000.
 - [20] T.A. Adami, J.J. Zhu, Flight control of hypersonic scramjet vehicles using a differential algebraic approach, in: Proceedings of the AIAA Guidance, Navigation, and Control Conference and Exhibit, AIAA 2006-6559, 2006.
 - [21] T.A. Adami, J.J. Zhu, Control of a flexible hypersonic scramjet vehicle using a differential algebraic approach, in: Proceedings of the AIAA Guidance, Navigation, and Control Conference and Exhibit, AIAA 2008-7464, 2008.
 - [22] Y. Liu, J.J. Zhu, Regular perturbation analysis for trajectory linearization control, in: Proceedings of the American Control Conference, 2007.
 - [23] Y. Liu, J.J. Zhu, Singular perturbation analysis for trajectory linearization control, in: Proceedings of the American Control Conference, 2007.
 - [24] R. Huang, Y. Liu, J.J. Zhu, Guidance, navigation, and control system design for tripropeller vertical-takeoff-and-landing unmanned air vehicle, *J. Aircr.* 46 (6) (2009) 1837–1856.
 - [25] Y. Liu, J.J. Zhu, R.L. Williams, J.H. Wu, Omni-directional mobile robot controller based on trajectory linearization, *Robot. Auton. Syst.* 56 (5) (2008) 461–479.
 - [26] Z.Q. Gao, Y. Huang, J.Q. Han, An alternative paradigm for control system design, in: Proceedings of the 40th IEEE Conference on Decision and Control, 2001.
 - [27] J.Q. Han, From PID to active disturbance rejection control, *IEEE Trans. Ind. Electron.* 56 (3) (2009) 900–906.
 - [28] J.Q. Han, Active Disturbance Rejection Control Technique – The Technique for Estimating and Compensating the Uncertainties, National Defense Industry Press, Beijing, 2009 (in Chinese).
 - [29] J.J. Zhu, PD-spectral theory for multivariable linear time-varying systems, in: Proceedings of the 36th IEEE Conference on Decision and Control, 1997.
 - [30] D.S. Naidu, A.J. Calise, Singular perturbations and time scales in guidance and control of aerospace systems: a survey, *J. Guid., Control, Dyn.* 24 (6) (2001) 1057–1078.
 - [31] D.S. Naidu, Analysis of non-dimensional forms of singular perturbation structures for hypersonic vehicles, *Acta Astronaut.* 66 (3–4) (2010) 577–586.
 - [32] H.K. Khalil, *Nonlinear Systems*, 3rd ed. Prentice Hall, New Jersey, 2002.
 - [33] J.Q. Han, R. Zhang, Error analysis of the second order ESO, *J. Syst. Sci. Math. Sci.* 19 (4) (1999) 465–471.
 - [34] Y. Huang, J.Q. Han, The self-stable region approach for second order nonlinear uncertain systems, in: Proceedings of 1999 IFAC World Congress, 1999.
 - [35] T. Yoshizawa, *Stability Theory and the Existence of Periodic Solutions and Almost Periodic Solutions*, Springer-Verlag, New York-Heidelberg-Berlin, 1975.
 - [36] C. Tunç, E. Tunç, On the asymptotic behavior of solutions of certain second-order differential equations, *J. Franklin Inst.* 344 (5) (2007) 391–398.



Zhiqiang Pu received his B.Eng. degree from Wuhan University in 2009. He is currently a Ph.D. candidate at the Institute of Automation, Chinese Academy of Sciences. His research interests include nonlinear robust control, adaptive control, and hypersonic vehicle guidance and control.



Xiangmin Tan received his B.Eng. degree from Central South University in 2004 and Ph.D. from the Graduate School of Chinese Academy of Sciences in 2009. He is currently an associate professor at the Institute of automation, Chinese Academy of Sciences. His research interests include hypersonic vehicle guidance and control, robotics, industrial control, and neural networks.



Guoliang Fan received his B.Eng. degree from Harbin Engineering University in 1997, M.S. degree from Harbin Institute of Technology in 2003, and Ph.D. degree from the Graduate School of Chinese Academy of Sciences in 2006. He is currently an associate professor at the Institute of automation, Chinese Academy of Sciences. His research interests include unmanned air vehicles, localization of aerial vehicle, flight control and autopilot.



Jianqiang Yi received his B.Eng. degree from the Beijing Institute of Technology, Beijing, China, in 1985, and his M.E. and Ph.D. degrees from the Kyushu Institute of Technology, Kitakyushu, Japan, in 1989 and 1992, respectively. He worked as a Research Fellow at the Computer Software Development Company, Tokyo, Japan, from 1992 to 1994, and a Chief Engineer at MYCOM, Inc., Kyoto, Japan, from 1994 to 2001. Since 2001 he has been with the Institute of Automation, Chinese Academy of Sciences, China, where he is currently a Professor. He is an Associate Editor for the Journal of Advanced Computational Intelligence and Intelligent Informatics, and the Journal of Innovative Computing, Information and Control. His research interests include theories and applications of intelligent control, intelligent robotics, under-actuated system control, sliding-mode control, flight control, etc.